

Analysis of Variations in Structure from High Resolution Electron Microscope Images by Combining Real Space and Fourier Space Information

Martin J. Hÿtch

Centre d'Études de Chimie Métallurgique, Centre National de Recherche Scientifique,
15 rue G. Urbain, 94407 Vitry-sur-Seine, France

(Received November 25; accepted December 6, 1996)

PACS.61.16.Bg – Transmission, reflection and scanning electron microscopy (including EBIC)

PACS.07.78.+s – Electron, positron, and ion microscopes, electron diffractometers,
and related techniques

PACS.42.25.Hz – Interference

PACS.42.30.Kq – Fourier optics

PACS.42.30.Rx – Phase retrieval

Abstract. — A new method is described for analysing variations in structure from high resolution electron microscope images. In Fourier theory, the image of a perfect crystal can be considered as the sum of sinusoidal lattice fringes having constant amplitude and phase given by the corresponding Fourier component. Imperfections are introduced by allowing these Fourier components to be a function of position, thus combining real space and reciprocal space information. It is shown how images can be obtained of the local value of the amplitude and phase of each major image periodicity. The amplitude and phase images are interpreted in terms of image detail and structural variations. Relationships are derived between the phase images and displacement fields due to a distortion of the lattice fringes and variations in the local reciprocal lattice vector. The meaning of the amplitude and phase images is illustrated by the analysis of experimental images of antiphase boundaries. Quantitative analysis of experimental images of carbon nanotubes is carried out using amplitude images and of strained metal multilayers using phase images.

1. Introduction

Fourier theory was first used to describe microscope optics by Duffieux [1] and is, otherwise, indispensable for the understanding of high resolution electron microscope images. This is because the image is not a simple representation of the specimen structure. Apart from dynamical scattering effects, the lens has too great an influence on the image. Each lattice fringe in the image is due to the interference of several beams, each combination being affected differently by the lens. Each beam is, in turn, affected to different extents by dynamical scattering. Only by analysing each periodicity in the image separately is it possible to appreciate these effects and hence to discern the underlying contribution due to the specimen structure.

High resolution electron microscopy is, however, less concerned with perfect structures than with departures from the norm, whether these being interfaces, defects, lattice distortions

or variations in chemistry. The problem with an analysis in Fourier space is that the real space information concerning these variations has been lost, for example, the position of a dislocation or the shape of a precipitate. On the other hand, an analysis in real space suffers from the fact that the effects of the lens and the diffraction are best understood in Fourier space. It would therefore be useful to be able to combine the information in real and reciprocal space in some way.

Gabor realized some time ago the limitations of an analysis carried out either entirely in real space or frequency space [2]. He was concerned with the analysis and perception of sound. A note in music, for example, needs to be understood in terms of both its pitch and its duration, each characteristic being equally important. The quantum mechanical equivalent is the description of a photon in terms of a wave packet having a carrier frequency and modulation. Gabor proposed to analyse images (or signals in his case) in terms of these wave packets [2]. The kq -representation proposed by Zak to describe electrons within solids is a similar example [3,4] and recently these two approaches have been combined into a more general formulation with applications in both optics and image processing [5]. Here we propose a method, developed independently, of combining real space and reciprocal space information by producing images of the local values of the Fourier components [6]. The method has been previously used to analyse high resolution images of nanocrystals [7] and can be considered as a specific case of the afore mentioned formulation. The emphasis here will be on the interpretation and the practical information that can be obtained from experimental images.

2. Image Decomposition

For the image of a perfect crystal, the intensity at a position \mathbf{r} on the screen, $I(\mathbf{r})$, can be written as a Fourier sum:

$$I(\mathbf{r}) = \sum_g H_g \exp\{2\pi i \mathbf{g} \cdot \mathbf{r}\} \quad (1)$$

where \mathbf{g} corresponds to a Bragg reflection and H_g the corresponding Fourier components. We can analyse the image in terms of the complex Fourier components H_g . Variations can be described by allowing these Fourier components to be a function of position, giving them a local value in the image, $H_g(\mathbf{r})$:

$$I(\mathbf{r}) = \sum_g H_g(\mathbf{r}) \exp\{2\pi i \mathbf{g} \cdot \mathbf{r}\}. \quad (2)$$

The Fourier transform of equation (2) gives the following relation:

$$\tilde{I}(\mathbf{k}) = \sum_g \tilde{H}_g(\mathbf{k} - \mathbf{g}). \quad (3)$$

In such a way, the Fourier transform of the image can be imagined as a convolution of the functions $\tilde{H}_g(\mathbf{k})$ with the reciprocal lattice vectors \mathbf{g} . The Fourier transform of the image $I(\mathbf{k})$ is effectively mapped out in terms of Brillouin zones. For a vector \mathbf{k} within a Brillouin zone centred on \mathbf{g} we can define that $\tilde{I}(\mathbf{k}) = \tilde{H}_g(\mathbf{k} - \mathbf{g})$. This is equivalent to defining that $\tilde{H}_g(\mathbf{k}) = 0$ for all values of \mathbf{k} beyond the first Brillouin zone. In this way $H_g(\mathbf{r})$ can be determined uniquely. Explicitly we can write this as:

$$\tilde{H}_g(\mathbf{k}) = \tilde{I}(\mathbf{k} + \mathbf{g}) \tilde{M}(\mathbf{k}) \quad (4)$$

where $\tilde{M}(\mathbf{k}) = 1$ inside the first Brillouin zone and zero outside.

2.1. Amplitude and Phase

We will be interpreting the complex images $H_g(\mathbf{r})$ in terms of their amplitude, $A_g(\mathbf{r})$, and phase, $P_g(\mathbf{r})$, defined by:

$$H_g(\mathbf{r}) = A_g(\mathbf{r}) \exp\{iP_g(\mathbf{r})\}. \quad (5)$$

The reason is not simply that complex images are difficult to understand but that, as will be shown, the amplitude and phase images are closely related to physically significant features in the original image.

Let us begin with considering Bragg filtering. The usual procedure to produce a Bragg filtered image, $B_g(\mathbf{r})$, is to place a mask around the spots $\pm\mathbf{g}$ in the Fourier transform of the image and then back-Fourier transform. Using equation (2), assuming the mask to be the shape of one Brillouin zone, the image intensity will be given by:

$$B_g(\mathbf{r}) = H_g(\mathbf{r}) \exp\{2\pi i\mathbf{g} \cdot \mathbf{r}\} + H_{-g}(\mathbf{r}) \exp\{-2\pi i\mathbf{g} \cdot \mathbf{r}\}. \quad (6)$$

It is easy to show that for a real image, $I(\mathbf{r})$:

$$H_g(\mathbf{r}) = H_{-g}^*(\mathbf{r}) \quad (7)$$

and therefore equation (6) becomes:

$$B_g(\mathbf{r}) = 2\Re [H_g(\mathbf{r}) \exp\{2\pi i\mathbf{g} \cdot \mathbf{r}\}] \quad (8)$$

where \Re denotes the real part. Expressing $H_g(\mathbf{r})$ in terms of an amplitude, $A_g(\mathbf{r})$, and a phase, $P_g(\mathbf{r})$, as defined in equation (5), we find that:

$$B_g(\mathbf{r}) = 2A_g(\mathbf{r}) \cos\{2\pi\mathbf{g} \cdot \mathbf{r} + P_g(\mathbf{r})\}. \quad (9)$$

This equation allows us to interpret the amplitude and phase images [7].

2.2. Amplitude Images

There are two levels to the interpretation. The first concerns the correspondence between the amplitude and phase images and aspects of the original image. The second is to interpret these details in terms of the structure of the specimen.

In terms of the image, the amplitude shows the degree of contrast of a set of fringes at a particular position in the image. Put another way, it is the envelope function which multiplies a set of perfect cosine fringes to produce the experimental fringes. The value obtained, though local, is an average over a region surrounding the position of interest with the amount of averaging determined by the size of the mask, $M(\mathbf{k})$, used in reciprocal space. The smaller the mask the larger the spatial extent of the averaging in real space, and *vice-versa*. For a mask of size equal to one Brillouin zone, the averaging will be carried out over approximately one unit cell. Depending on the noise present in the image, we may be obliged to use a smaller size of mask and approximate the functions $H_g(\mathbf{r})$ by greater averaging. In that case the lateral resolution of the amplitude image will be reduced.

In terms of the specimen, the amplitude variations could be due to changes in the thickness of the specimen, the chemical composition, or the imaging conditions. Qualitatively, it will often be possible to distinguish between these various effects because of the different length scales involved and by combining information from other sets of fringes. To obtain quantitative results, as always with high resolution electron microscopy, the amplitude images need to be compared with the results obtained with simulations. In this way, the questions concerning the size of the mask become irrelevant. The same mask is used for the simulations and the only criteria is the similitude with the experimental results. An example will be given later.

2.3. Phase Images

The phase images represent the deviation of the fringes in the image from their ideal positions. This can be demonstrated by beginning with the equation for a perfectly regular set of fringes:

$$B_g(\mathbf{r}) = 2A_g \cos\{2\pi\mathbf{g} \cdot \mathbf{r} + P_g\} \quad (10)$$

where the amplitude and phase is no longer a function of position. For a distorted image, the Bragg fringes of equation (10) can be written:

$$B_g(\mathbf{r}) = 2A_g \cos\{2\pi\mathbf{g} \cdot \mathbf{r} - 2\pi\mathbf{g} \cdot \mathbf{u}\} \quad (11)$$

where \mathbf{u} is the displacement field. This can be understood by considering the position of the fringe maxima which, if before they were at position \mathbf{r} , will now be at a position $\mathbf{r} + \mathbf{u}$. Comparing equation (11) with equation (9) gives the following relation between the phase and the displacement field:

$$P_g(\mathbf{r}) = -2\pi\mathbf{g} \cdot \mathbf{u}. \quad (12)$$

The component of the displacement field, $u_g(\mathbf{r})$, in the direction \mathbf{g} can therefore be measured from the phase image. Combining results from other directions will give the vectorial displacement field.

In principle, the displacement field could also be measured using a different set of periodicities in the image. In order that the results are consistent with each other, the following rule can be defined:

$$P_g(\mathbf{r}) = P_{g-g'}(\mathbf{r}) + P_{g'}(\mathbf{r}) \quad (13)$$

which is easily verified by substituting equation (12). In practice, this equation will never be satisfied exactly, given the approximations involved in the interpretation of the phase in terms of a displacement field and due to the presence of noise. It therefore serves as a very useful test as to the validity of the interpretation.

If the fringes in the image vary in spacing, the ideal set of fringes of equation (10) will become:

$$B_g(\mathbf{r}) = 2A_g \cos\{2\pi\mathbf{g} \cdot \mathbf{r} + 2\pi\Delta\mathbf{g} \cdot \mathbf{r}\} \quad (14)$$

where $\Delta\mathbf{g}$ is the local departure from the ideal reciprocal lattice vector \mathbf{g} . Comparing this equation with equation (9) we find that:

$$P_g(\mathbf{r}) = 2\pi\Delta\mathbf{g} \cdot \mathbf{r}. \quad (15)$$

A gradient in the phase can therefore be interpreted as a local change in the reciprocal lattice vector. This can be expressed mathematically by taking the gradient of equation (15):

$$\nabla P_g(\mathbf{r}) = 2\pi\Delta\mathbf{g}. \quad (16)$$

This result is linked to the previous one: the gradient of the displacement field gives the local lattice spacing.

What is true for the amplitude is true for the phase: the positions of the fringes in the image do not necessarily correspond to the positions of the atomic planes. The phase images are affected in exactly the same way as the amplitude by the size of mask used in Fourier space and by the aberrations of the lens. However, the conditions for simple interpretation of the phase are less restrictive than for the amplitude images for medium-range variations between 1 and 10 nm. For example, in the absence of misalignments, variations in thickness do not shift the positions of the fringes in the image. For longer-range variations the distortions introduced by the projector lenses become important [8] as do variations in the imaging conditions. A fuller discussion of these points can be found elsewhere [6].

2.4. Method of Reconstruction

The complex images $H_g(\mathbf{r})$ are calculated using the equation (4). This could be carried out in practice by recentring the Fourier transform of the image, applying the mask, and back-Fourier transforming. A digitized image is not however a continuous function which means that the Fourier transform cannot be recentred exactly on the position \mathbf{g} , this position being in general between pixels [9]. To avoid this problem the mask is placed around the periodicity of interest and the back-Fourier transform taken without recentring. Referring to equation (2), the complex image produced, $H'_g(\mathbf{r})$, will be given by:

$$H'_g(\mathbf{r}) = H_g(\mathbf{r}) \exp\{2\pi i \mathbf{g} \cdot \mathbf{r}\}. \quad (17)$$

The Bragg, amplitude and phase images are then calculated from this image in the following way:

$$2\Re [H'_g(\mathbf{r})] = B_g(\mathbf{r}) \quad (18)$$

$$\text{Mod} [H'_g(\mathbf{r})] = A_g(\mathbf{r}) \quad (19)$$

$$\text{Phase} [H'_g(\mathbf{r})] = P_g(\mathbf{r}) + 2\pi \mathbf{g} \cdot \mathbf{r} \quad (20)$$

where to obtain the phase image, the factor of $2\pi \mathbf{g} \cdot \mathbf{r}$ is subtracted and the results renormalized between $\pm\pi$. All the image processing and image simulation presented in this paper was carried out using procedures written within the image processing package SEMPER [10].

The operation is identical to a holographic reconstruction with the periodicity \mathbf{g} taken as the carrier wave. The amplitude and phase recovered here though refers to the image, the term geometric phase is sometimes employed to emphasis this fact [6, 7]. To obtain the amplitude and phase of periodicities in the electron wavefunction it is necessary to analyse an electron hologram, as proposed by Scheerschmidt and Knoll [11].

3. Antiphase Boundaries

The first example illustrates the kind of qualitative analysis that can be carried out by combining real space and reciprocal space information, and should clarify the meaning of the amplitude and phase images. Figure 1a shows a high resolution image of long-range ordered CoPt_3 ($a = 0.38$ nm) in [001] projection taken on a JEOL 4000FX operating at 400 kV (courtesy of Christian Ricolleau). In the perfectly ordered structure, planes of pure Pt alternate with planes rich in Co. An objective aperture was used to exclude all but the spots $\{100\}$ and $\{110\}$ due to this ordering. In the image we therefore only see one set of planes, either the planes rich in Co or the planes of pure Pt, depending on the thickness and defocus. Antiphase domains are revealed in the image by the relative displacement of the fringes due to this ordering by half a unit cell. Wetting of the antiphase boundaries has occurred, however, so there is a zone of disordered material separating the long range ordered domains (for a review of this subject see [12]).

Figure 2 shows how the information in the image can be decomposed. The Bragg filtered image corresponding to the 100 fringes is seen in Figure 2a. The mask used was Gaussian in shape and positioned on the 100 spot in the Fourier transform of the image as shown in Figure 1b. For this example we have used the same Gaussian shape as proposed by Gabor:

$$\tilde{M}(\mathbf{k}) = \exp \left\{ -4\pi \frac{k^2}{g^2} \right\}. \quad (21)$$

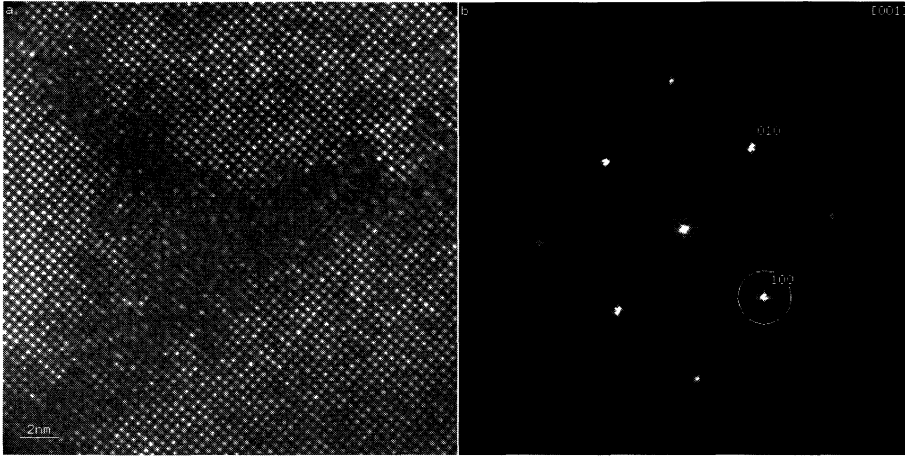


Fig. 1. — Antiphase domains in CoPt_3 : a) high resolution image (courtesy of Christian Ricolleau); b) power spectrum of the image with 100 mask indicated.

The shape of the mask is not of great importance for this example because the analysis is qualitative. A Gaussian shape will give a smoother aspect to the final image than a hard edged square mask and the size of the mask will determine the averaging carried in real space. In this case, the effectiveness of a particular mask is determined by whether the details of interest are visible in the final image and will depend on the signal to noise ratio. The Bragg filtered images show continuous, straight fringes which shift by half a fringe spacing across the antiphase boundaries. When a larger mask was tried, the fringes lost this continuous aspect because of the noise in the original image.

The amplitude images are the most easily understood. The amplitude of the 100 or 010 fringes do not vary much within a particular antiphase domain, the implication being that the crystal thickness and composition are relatively constant. The mottled contrast is predominantly due to noise. The antiphase boundaries appear as wide black lines of zero amplitude (compare, for example, Figs. 2a, b) because the $\{100\}$ periodicity disappears due to the disordering. The amplitude images can be interpreted in a similar way to dark-field images taken for the corresponding reflection with the important difference that both the $\pm\mathbf{g}$ beams and the straight through beam contribute to the image contrast. Measuring the widening of the interfaces due to wetting from the amplitude images would be an improvement on visual inspection of the original image contrast.

The translation domain structure is revealed by the phase images as regions of black or white contrast. Within a particular domain, the phase is relatively constant which means that the fringes are almost perfectly spaced, straight and without distortion. Across the antiphase boundary the positions of the fringes shift by half a unit cell which corresponds to a phase change of π , hence the black/white binary contrast. Combining the information from the 100 and 010 phase images, the vectorial translation domain map can be obtained according to Table I. An image can even be constructed (Fig. 3) using the formula $P_{010}(\mathbf{r}) - \frac{1}{2}P_{100}(\mathbf{r})$ where the grey levels correspond to the four translation domains. A more complete study of antiphase boundaries using phase images can be found elsewhere [13].

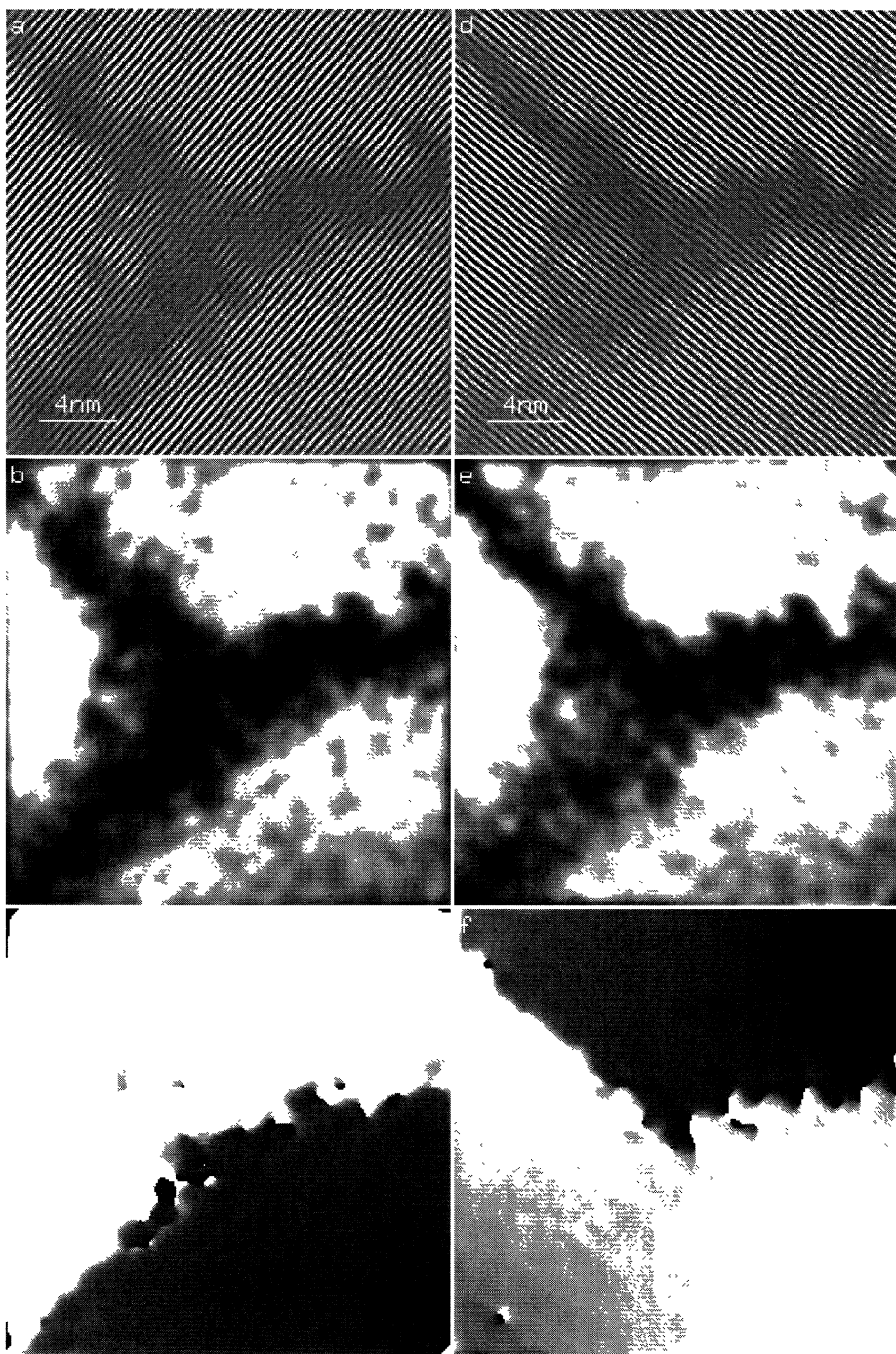


Fig. 2. — Decomposition of image of antiphase domains: a) 100 Bragg filtered image, $B_{100}(\mathbf{r})$; d) 010 Bragg filtered image, $B_{010}(\mathbf{r})$; b) 100 amplitude image, $A_{100}(\mathbf{r})$; e) 010 amplitude image, $A_{010}(\mathbf{r})$; c) 100 phase image, $P_{100}(\mathbf{r})$, black = 0 white = 2π ; f) 010 phase image, $P_{010}(\mathbf{r})$, black = 0 white = 2π .

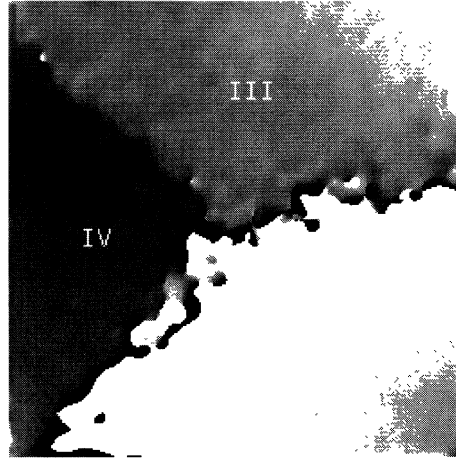


Fig. 3. — Translation domain structure. Domain types refer to Table I.

Table I. — *Interpretation of phase in terms of translation domains.*

Translation Domain	Phase			Translation Vector
	100	010	110	
I	0	0	0	000
II	0	π	π	$0\frac{1}{2}\frac{1}{2}$
III	π	0	π	$\frac{1}{2}0\frac{1}{2}$
IV	π	π	0	$\frac{1}{2}\frac{1}{2}0$

3.1. Antiphase Boundaries in Cu_3Au

The example of antiphase domains, apart from providing a demonstration of the meaning of amplitude and phase images, can also provide arguments for justifying the analyse of each image periodicity separately.

Figure 4 shows a high resolution image of an antiphase boundary in Cu_3Au where a much larger objective aperture was used which included the $\{300\}$ reflections (courtesy of Laurence Potez). With the higher resolution detail present, the antiphase boundary is more difficult to see. Indeed, if the atomic structure of the boundary was of interest, reducing the resolution of the image, as in the previous example, would be counter-productive. The phase images, however, clearly reveal the antiphase boundary as before (Figs. 4c, d). Phase profiles across the boundary could be used to analyse the abruptness of the interface and possible strain fields present according to equation (12). These possibilities will not be pursued further here but what is of interest is that the apparent position of the boundary is not the same for the two sets of fringes (Figs. 4c, d). It is displaced by 1.4 ± 0.2 unit-cells or 0.5 ± 0.1 nm. How could this be?

The simplest explanation is that some beam tilt is present which can shift the position of fringes in the image by adding a phase factor proportional to $\mathbf{g} \cdot \mathbf{t}$ where \mathbf{t} is the beam tilt [14]. If more beam tilt is present in the 110 direction than the 100, these two sets of fringes will be shifted with respect to each other. In the image therefore, which is a sum of all the sets

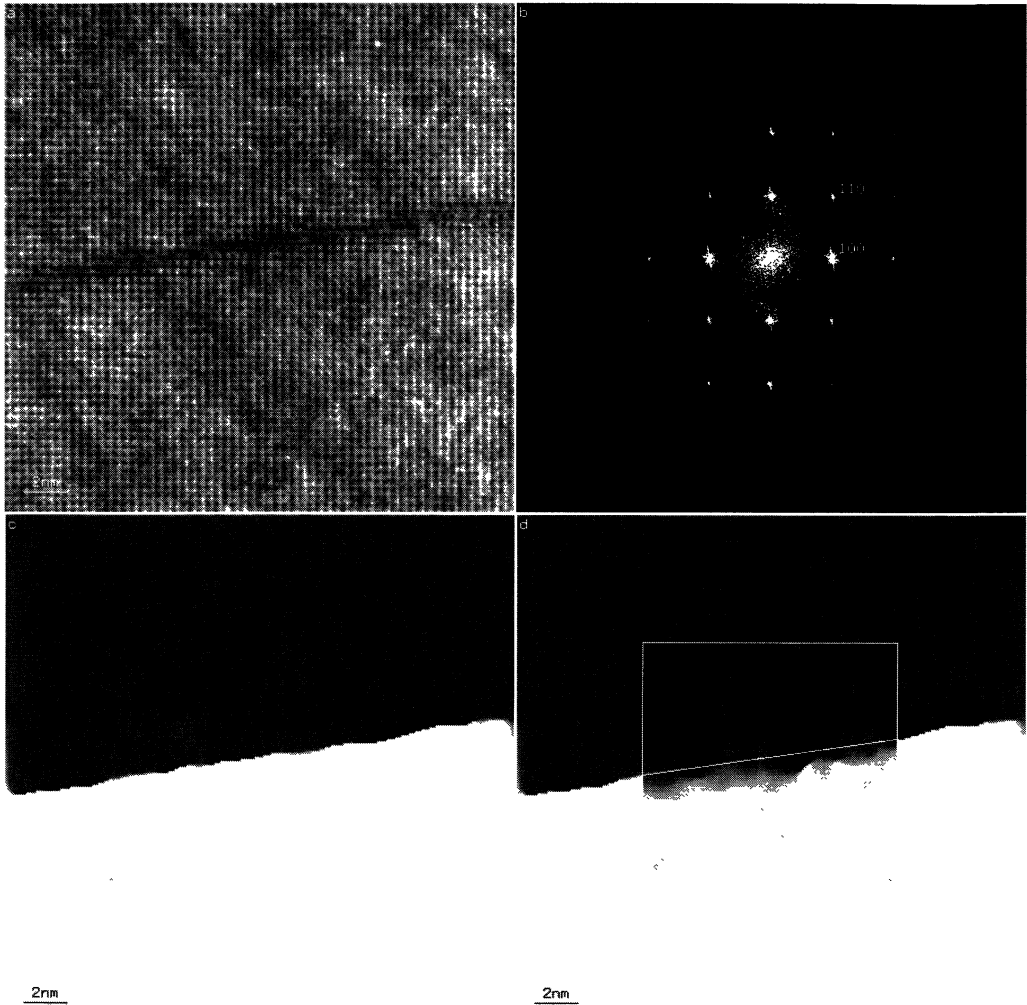


Fig. 4. — Antiphase boundaries in the presence of beam tilt: a) high resolution image of Cu_3Au in $[001]$ projection (courtesy of Laurence Potez); b) power spectrum of image; c) 100 phase image, $P_{100}(\mathbf{r})$, black = 0 white = 2π ; d) 100 phase image with 110 phase image, $P_{110}(\mathbf{r})$, inserted. White line indicates position of antiphase boundary for 100 phase. The apparent position of the antiphase boundary for the 110 phase image is shifted by 0.5 ± 0.1 nm with respect to the 100 phase.

of fringes, the interface will appear diffuse. By analysing the individual image components we can see that this is not true. Indeed, we are not prevented from continuing the study the abruptness of the interface by using the phase profiles.

These conclusions are valid for any type of interface. It is often the case that the variation at the interface affects certain periodicities more than others. Decomposing the image information therefore focussed attention on the most important variations, and thus revealing the position and shape of the interface more clearly. In the presence of misalignments the interface is *necessarily* more diffuse in the image than in reality. Any method which analyses all the image fringes simultaneously will encounter this problem. Decomposing the image information avoids this problem and allows further analysis.

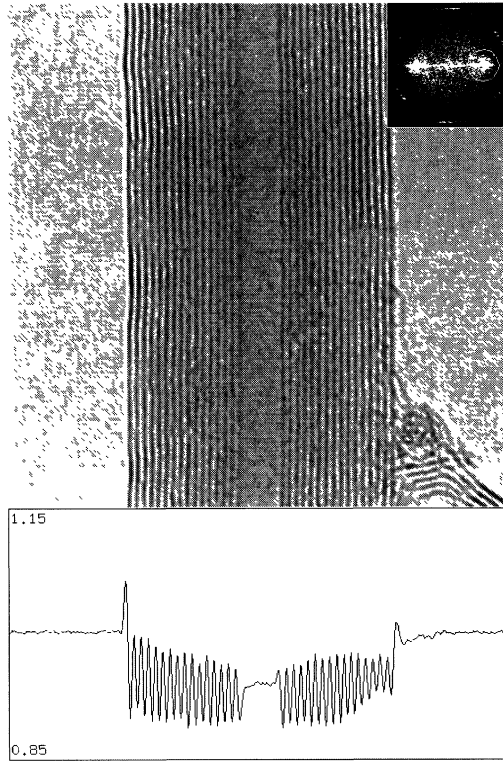


Fig. 5. — High resolution image of 16-shell carbon nanotube (courtesy of P. Ajayan). Power spectrum inset shows mask used for 0002 fringes. Intensity profile, averaged along the length of the tube, also shown. Incident intensity = 1.

4. Carbon Nanotubes

The quantitative use of amplitude images is illustrated in the following example. Figure 5 shows a high resolution image of a 16-shell carbon nanotube taken on a TOPCON 002B microscope operating at 200 kV (courtesy of P. Ajayan). The structure corresponds to a set of nested cylinders of graphene, the spacing between successive layers being roughly equivalent to that in graphite (0.36 nm). The high resolution images are not easily understood without the help of simulations. For example, the image appears like a cross-section through the structure with parallel 0002 fringes corresponding to the outer edge of each graphene cylinder. This is surprising and indeed such images were initially interpreted as corresponding to 2-dimensional structures. Neither is the number of shells in the tube immediately obvious, given that the contrast could be positive or negative. It is therefore important to be able to construct a model for the nanotube and then to compare the corresponding simulated images with the experimental results.

The model, which will be tested here, is non-atomistic and consists of concentric cylinders of graphene with perfectly circular cross-sections [15,16]. The atoms of carbon were assumed to be uniformly distributed over the surface of each cylinder with a density equal to that of a graphene sheet. The exit wavefunction was calculated from the projected potential using the phase object approximation and simulations performed (accelerating voltage 200 kV, $C_s = 0.4$ mm, beam

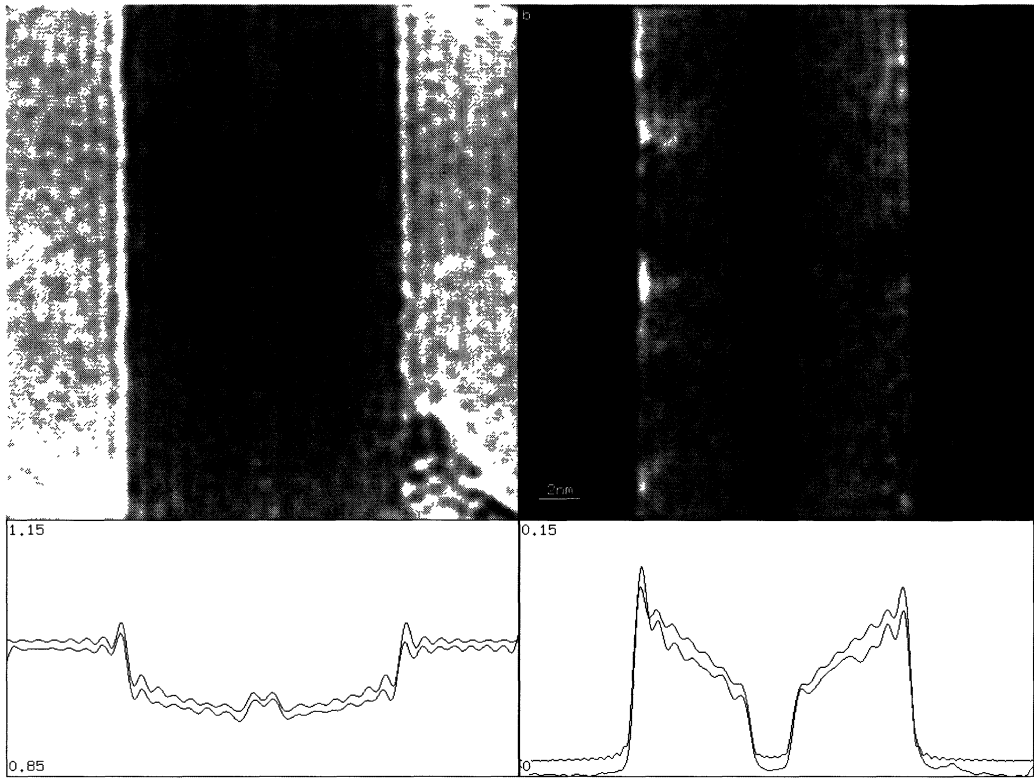


Fig. 6. — Amplitude images with corresponding line profiles averaged along the length of the tube: a) local mean intensity, $A_0(\mathbf{r})$; best fitting simulated line profile also shown (defocus -30 nm) but displaced vertically with respect to experimental profile for display purposes; b) 0002 amplitude image, $A_{0002}(\mathbf{r})$; best fitting simulated line profile (defocus -30 nm) also shown and displaced vertically. Incident intensity = 1.

divergence 1 mrad, focal spread 10 nm). The comparison with the experimental results was carried out in terms of the individual Fourier components, comparing the results from each periodicity in turn. Comparing the average intensity profile, shown in Figure 5, directly with profiles from the simulated data is not useful; the reasons should become clear during the following analysis.

Two amplitude images were analysed, $A_{0002}(\mathbf{r})$, the amplitude of the 0002 fringes (Fig. 6b) and $A_0(\mathbf{r})$, produced by placing a mask around the central peak of the Fourier transform of the image (Fig. 6a). The latter is the same as a low-pass filtered image and can be interpreted as showing the variation in the local mean intensity in the image. Line profiles, averaged along the length of the nanotube, show the variations more clearly (see Fig. 6). There are three main effects producing the image details: diffraction contrast, Fresnel fringe contrast and absorption contrast. The 0002 fringes are almost entirely due to diffraction contrast, whereas the variations in the mean contrast, $A_0(\mathbf{r})$, are due to Fresnel fringe contrast (at the edges of the tube where the mean inner potential changes rapidly) and absorption contrast.

A carbon nanotube acts like an almost perfect phase object. Given the projected potential, the only imaging parameter needed (apart from the beam divergence and focal spread) is the defocus. To determine this, the experimental 0002 fringe amplitude, $A_{0002}(\mathbf{r})$, with simulated

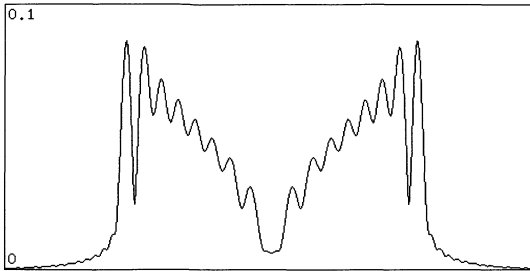


Fig. 7

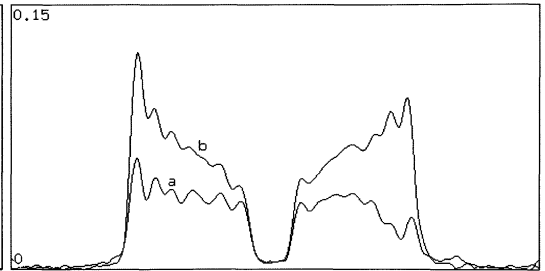


Fig. 8

Fig. 7. — Simulated 0002 amplitude profile for a defocus of -80 nm. Incident intensity = 1.

Fig. 8. — Comparison between 0002 amplitude line profiles corresponding to: a) intensity profile obtained by averaging original experimental image along the tube length (Fig. 5); b) amplitude image averaged along the tube length (as in Fig. 6b).

profiles at different values of defocus, Figure 7 shows an example. The behaviour at the edge of the tube is sensitive to the defocus, and in this way the defocus was found to good accuracy to be -30 ± 5 nm. The best fit obtain, shown in Figure 6, shows how well the details of the experimental image are reproduced.

The absorption contrast was modelled by adding an imaginary part to the potential, proportional to the real potential. The value of the absorption parameter, α , is not known in general and was therefore varied until the best fit was found between the experimental and simulated $A_0(\mathbf{r})$ profiles (Fig. 6a). The Fresnel fringes at the edge of the tube depend on the defocus (determined previously) and are almost independent of the absorption. In this way, the value of absorption can be determined uniquely. By separating the image detail into 0002 and mean intensity contrast it is thus possible to determine the simulating parameters separately.

When analysing absolute intensities, special care must be taken with averaging. Figure 8 compares the amplitude of the 0002 fringes in the intensity profile obtained by averaging the original image (Fig. 5) and by averaging the amplitude image (Fig. 6b). Between 40% and 70% of the contrast has been lost on averaging the original image. This is because the graphene layers are not straight, there is a significant roughness and the tube is slightly bent. This can be seen in the original image and can be measured from the phase image for the 0002 fringes [6]. In comparing absolute levels of contrast it is therefore essential to use the averaged amplitude image profiles (Fig. 6).

The experimental fit obtained in Figure 6 was only obtained by reducing the simulated contrast. The simulated $A_0(\mathbf{r})$ was reduced by a factor of 1.5 and the simulated $A_{0002}(\mathbf{r})$ by a factor 3.3. It would have therefore been very difficult to match the overall contrast (Fig. 5), a different factor being necessary for the two aspects of the image. It seems that the reduction of the overall contrast of 1.5 is due to a significant number of electrons forming an incoherent background, possibly due to scattering to high angles. The additional reduction of amplitude of the 0002 fringes by a factor of 2.2 can be explained by proposing that the graphene layers have a roughness of 0.07 nm around the tube axis. Roughness on a similar scale has been reported using scanning tunnelling electron microscopy [17]. A more detailed examination of these effects has been carried out elsewhere [15,16]. What is important here is that without the amplitude images it would have been impossible to discuss these effects and to propose a quantitative model as a solution. It has also been possible to show that the model reproduces the experimental details to a high degree of accuracy.

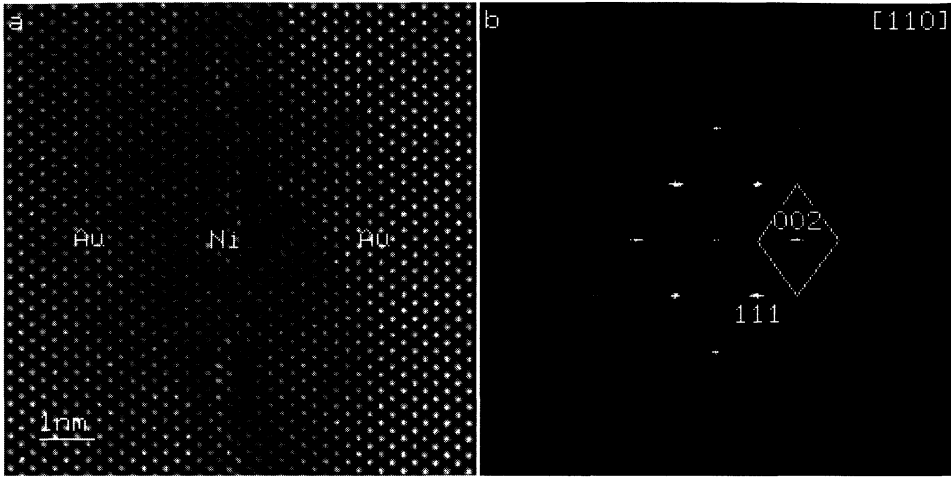


Fig. 9. — Strained metal multilayers: a) high resolution image of Au/Ni multilayer (courtesy of Pascale Bayle) Ni layer lies vertically and is nominally two atomic planes wide, growth direction is from left to right; b) power spectrum of image with mask for 002 fringes marked.

5. Strained Metal Multilayers

The next example shows the use of the phase images to reveal changes in the local lattice parameter. Figure 9a shows a high resolution image, taken on a JEOL 4000EX microscope operating at 400 kV, at [110] incidence of an Au/Ni multilayer grown by molecular beam epitaxy (courtesy of Pascale Bayle). Lying vertically at the centre of the image is a Ni layer, nominally two atomic layers wide. The bulk lattice parameter of Ni is 14% less than that of Au so we would expect to see variations in the lattice fringe spacings in the image. Similar strained multilayers have been analysed by marking the positions of the peaks in intensity in the image, the separation of the peaks giving the local lattice fringe parameter [18–20]. The phase images should provide similar information given the relationship between the gradient of the phase and the local difference in reciprocal lattice fringe vector.

The image was therefore decomposed in terms of Bragg filtered images, amplitude and phase images for the 002, 111 and $\bar{1}\bar{1}1$ fringes (Fig. 10) using the mask shown in Figure 9b [21]. Neither the Bragg filtered nor the amplitude images show clearly the Ni layer. The phase images, however, reveal the presence of the Ni layer both by the difference in phase between the two Au layers and by an abrupt change in the gradient (see the line profiles in Figure 10(iv) taken across the phase images, averaged along the length of the layer).

A gradient in the phase means a difference in the local reciprocal lattice vector from that of the reference as given by equation (16). The reference lattice was taken from the Au layer to the right, so the phase is flat here. The step increase in the phase occurs at the Ni layers. According to calculations based on elastic theory, the Ni (001) lattice parameter should be reduced by a further 19% with respect to the Au lattice parameter [20]. This elastic compression comes from the fact that, for thin Ni layers, the (100) and (010) lattice parameters are constrained to that of Au (0.405 nm). The 002 fringe spacing should therefore be 29% shorter than that of Au and the difference in the local reciprocal lattice vector $\Delta\mathbf{g}_{002}$ from the reference Au lattice will be equal to $0.40\mathbf{g}_{002}^{\text{Au}}$. The positive gradient in the phase testifies to an increase in the local reciprocal lattice vector. To quantify this, $\Delta\mathbf{g}_{002}$ was calculated from

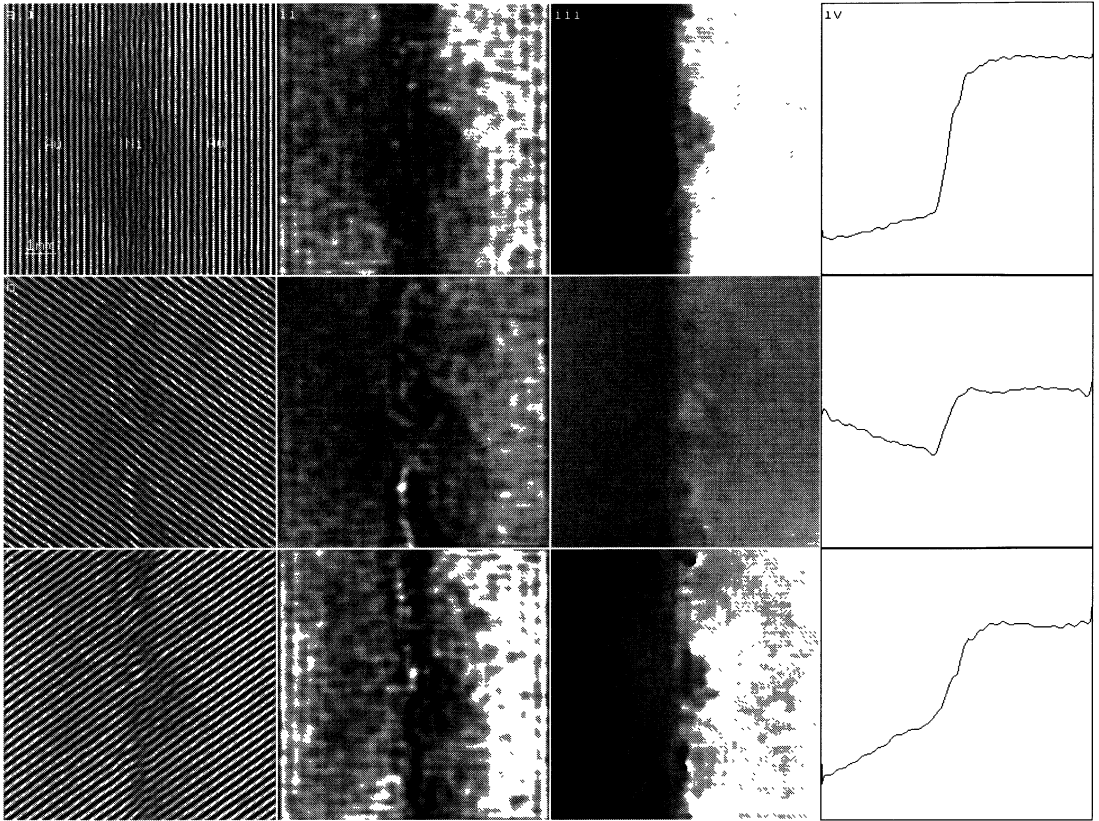


Fig. 10. — Decomposition of Au/Ni multilayer image: column (i) Bragg filtered images, $B_g(\mathbf{r})$; (ii) amplitude images, $A_g(\mathbf{r})$; (iii) phase images, $P_g(\mathbf{r})$, black = 0 white = 2π ; (iv) phase profiles average vertically. Row (a) 002 fringes; (b) $1\bar{1}1$ fringes; (c) 111 fringes.

the phase gradient using equation (16) and plotted as a function of position across the layers (Fig. 11). (Note, that this is only the component in the 002 direction.) It can be seen that the deviation never achieves the expected value of 40% of the Au reciprocal lattice vector.

It has been proposed that this is because of an intermixing of the Ni and the Au [20]. According to Vegard's law the lattice parameter, d_{001} , of a mixed compound is given by:

$$d_{001} = (1 - \rho_{\text{Ni}})d_{001}^{\text{Au}} + \rho_{\text{Ni}}d_{001}^{\text{Ni}} \quad (22)$$

where ρ_{Ni} is the proportion of Ni, and d_{001}^{Au} and d_{001}^{Ni} are the bulk parameters of Au and Ni respectively. For small deviations, the Ni concentration can therefore be approximated by the following relation:

$$\rho(\mathbf{r}) \simeq \frac{\Delta g_{002}}{0.40g_{002}^{\text{Au}}} \quad (23)$$

and so Figure 11 gives an indication of the concentration of Ni as a function of position in the image.

It is important to stress that this is only an approximation. Vegard's law has been assumed and the relaxation of the strained layers in a thin film has been ignored [22]. Most importantly, it has been assumed that the local lattice spacing in the image corresponds to that in the crystal

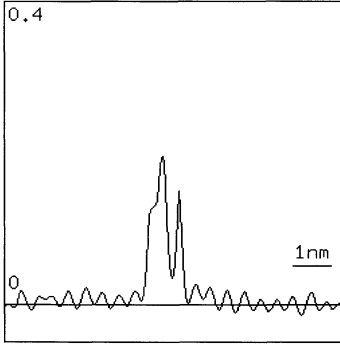


Fig. 11

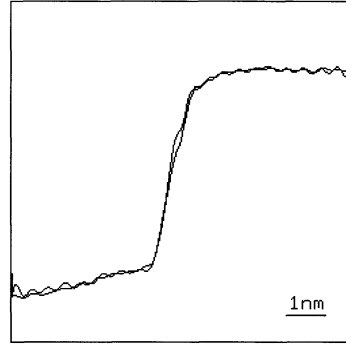


Fig. 12

Fig. 11. — Local reciprocal lattice vector, g_{002} , as a function of position across the layers expressed as a fraction of g_{002}^{Au} . For a pure Ni layer the expected value is $0.4g_{002}^{\text{Au}}$.

Fig. 12. — Consistency rule, equation (27), for testing results obtained from 002 phase image: 002 phase profile from $P_{002}(\mathbf{r})$ compared with profile obtained from $P_{111}(\mathbf{r}) + P_{\bar{1}\bar{1}\bar{1}}(\mathbf{r})$.

which is only true in the limit of slowly varying displacement fields, notably because of the effect of the lens. The composition profile shown in Figure 11 is a nice example: it is unlikely that the Ni concentration should dip in the middle of the layer. Bayle *et al.* [20] have shown that using simulated images based on perfectly reasonable concentration profiles, exactly this kind of behaviour is reproduced at certain defoci. The most likely explanation is the effect of the lens, similar to the results for the carbon nanotubes viewed at different defoci (Fig. 7). The correct procedure is therefore to obtain a good first estimate of the composition profile from the experimental image, model the layer system taking into account such effects as relaxation [19], and compare the simulations with the experimental data, refining the model as necessary [20].

The total amount of Ni can, however, be determined with much less difficulty, directly from the experimental phase image and is given by the difference in phase between the two Au layers, ΔP_{002} , seen in Figure 10(iv)a. The two Au layers are rigidly displaced with respect to each other because the Ni layers have a different lattice parameter. From equation (12) we have that:

$$\Delta P_{002} = -2\pi g_{002}^{\text{Au}} u_{002} \quad (24)$$

where u_{002} is the component of the rigid displacement perpendicular to the layers. Assuming that Vergard's law applies, we have that:

$$u = n(d_{002}^{\text{Ni}} - d_{002}^{\text{Au}}) = 0.29nd_{002}^{\text{Au}} \quad (25)$$

where n is the number of whole atomic layers of Ni. Note, that the Ni concentration can be spread out over any number of planes, this is the integrated result. Using equations (24, 25), and the fact that $g_{002}^{\text{Au}} = 1/d_{002}^{\text{Au}}$ we have that:

$$n = \frac{1}{0.29} \frac{\Delta P_{002}}{2\pi} . \quad (26)$$

The experimental result is $n = 2.05 \pm 0.05$. This result is affected much less by the experimental imaging conditions, unlike the measure of the local composition. For example, the lens has no effect on the measure if the thickness of the specimen is constant.

Similar results should be obtained from the 111 and $1\bar{1}\bar{1}$ fringes but looking at Figures 10b and 10c it seems that the phase profiles are significantly different. This is, however, primarily because there is a difference in the phase gradient between the two Au layers. The phase gradient is uniform which means that there is a rigid distortion of one layer with respect to the other. This can even be seen in the 002 phase where there is a difference in $0.5 \pm 0.1\%$ in the lattice fringe parameter. The high sensitivity of the phase measurements can be appreciated with this example and explains why the distortion is not noticeably in the original image (Fig. 9a). It would be interesting to carry out a systematic study of the distortion of the Au layers as a function of growth using the phase images.

For consistency, as defined by equation (13):

$$P_{002}(\mathbf{r}) = P_{111}(\mathbf{r}) + P_{1\bar{1}\bar{1}}(\mathbf{r}). \quad (27)$$

Comparison of the two sides of this equation, Figure 12, shows that there is very good agreement and where there are differences this is consistent with the earlier expectations. For example, the biggest differences are at the Ni layer where the lens effects are going to be important. The height of the step in the phase, however, remains unchanged.

6. Conclusions

When analysing a high resolution image of a variation in structure, it is important to consider each image periodicity separately. The influence of the lens is not the same for each lattice fringe in the image and the physical causes behind the experimental contrast may differ. The example of the images of carbon nanotubes demonstrated this clearly. The amplitude images allowed the separation of the diffraction contrast from that due to absorption and Fresnel fringe contrast, and showed the effect of defocus on the image contrast, thus allowing a refinement of the model and determination of the imaging parameters. The example of antiphase boundaries showed that in the presence of misalignments, an interface will always appear more diffuse in the original image than in reality, except where isolated image periodicities are concerned.

The displacement field corresponding to a distortion of the lattice fringes can be determined directly from the phase images as can changes in the local reciprocal lattice vector. The influence of the lens is much less important than for the amplitude images. For qualitative use of the phase images, antiphase domains can thus be identified as can the individual layers within a strained multilayer. For rapid variations in structure, the experimental results must be compared with simulations, as always with high resolution electron microscopy. For the examples studied here, this was best carried out in terms of the amplitude and phase images and not the original image; it is proposed that this will generally be the case. With the help of a consistency rule for the phase, it is even possible to assess the magnitude of image artefacts by considering different image periodicities. It should also be noted that averaging is best carried out on amplitude images and phase images and not the image, otherwise errors of more than 50% can be introduced into the measurements. Amplitude and phase images therefore not only help the interpretation of image contrast but can be used to quantitatively describe variations in specimen structure.

Acknowledgments

The author is indebted to Christian Ricolleau, Laurence Potez, Pulickel Ajayan and Pascale Bayle for the experimental results presented in this paper. It is also a pleasure to thank Jean-Pierre Chevalier for useful discussions and the use of the laboratory facilities at Vitry.

References

- [1] Duffieux P.-M., *L'intégrale de Fourier et ses applications à l'optique* (Les Imprimeries Oberthur, Rennes, 1946).
- [2] Gabor D., *Proc. Inst. Electr. Eng.* **93** (1946) 429.
- [3] Zak J., *Phys. Rev.* **168** (1968) 686.
- [4] Zak J., *Solid State Phys.* **27** (1972) 1.
- [5] Bastiaans M.J., *Appl. Opt.* **33** (1994) 5241.
- [6] Hýtch M.J., in "Scanning Microscopy Supplement 10: Signal and Image Processing in Microscopy and Microanalysis", P. Hawkes, Ed. (Scanning Microscopy International, Chicago, 1996).
- [7] Hýtch M.J. and Gandais M., *Philos. Mag. A* **72** (1995) 619.
- [8] de Ruijter W.J. and Weiss J.K., *Ultramicroscopy* **50** (1993) 269.
- [9] Volk E., Allard L.F., Datye A. and Frost B., *Ultramicroscopy* **58** (1995) 97.
- [10] Saxton W.O., Pitt T.J. and Horner M., *Ultramicroscopy* **4** (1979) 343.
- [11] Scheerschmidt K. and Knoll F., *Phys. Stat. Sol. (a)* **146** (1994) 491.
- [12] Ricolleau C., Loiseau A. and Ducastelle F., *Phase Transitions* **30** (1991) 243.
- [13] Hýtch M.J. and Potez L., *Philos. Mag. A* (1997) accepted.
- [14] Smith D.J., Saxton W.O., O'Keefe M.A., Woods G.J. and Stobbs W.M., *Ultramicroscopy* **11** (1983) 263.
- [15] Hýtch M.J., Redlich P. and Ajayan P., in "Proc. European Electron Microscopy Meeting", EUREM 96 (Dublin, 1996).
- [16] Hýtch M.J., Redlich P. and Ajayan P., *Phys. Rev. B*, submitted (1996).
- [17] Hiura H., Ebbesen T.W., Fujita J., Tanigaki K. and Takada T., *Nature* **367** (1994) 148.
- [18] Bierwolf R., Hohenstein H., Philipp F., Brandt O., Crook G.E. and Ploog K., *Ultramicroscopy* **49** (1993) 273.
- [19] Jouneau P.H., Tardot A., Feuillet B., Mariette H. and Cibert J., *J. Appl. Phys.* **75** (1994) 7310.
- [20] Bayle P., Deutsch T., Gilles B., Lançon F., Marty A. and Thibault J., *Ultramicroscopy* **56** (1994) 94.
- [21] Hýtch M.J. and Bayle P., in "13th International Conference on Electron Microscopy" (Les Éditions de Physique, Les Ulis, 1994) Vol. 2A, pp. 129–30.
- [22] Treacy M.M.J. and Gibson J.M., *J. Vac. Sci. Technol. B* **4** (1986) 1458.